Operando real-space imaging of a structural phase transformation in a high-voltage electrode

Yifei Sun[1], Sunny Hy[2], Nelson Hua[3,4], James Wingert[3], Ross Harder[5], Ying Shirley Meng[2,6], Oleg Shpyrko[3], Andrej Singer[1,]*

[1]*Department of Materials Science and Engineering, Cornell University, Ithaca, New York 14850, USA*
[2]*Department of Nanoengineering, University of California San Diego, La Jolla, California, 92093, USA*
[3]*Department of Physics, University of California San Diego, La Jolla, California, 92093, USA*
[4]*Laboratory for X-ray Nanoscience and Technologies, Paul Scherrer Institut, 5232 Villigen, Switzerland*
[5]*Advanced Photon Source, Argonne National Laboratory, Argonne, Illinois, 60439, USA*
[6]*Pritzker School of Molecular Engineering, University of Chicago, Chicago, Illinois, 60637, USA*
[*]asinger@cornell.edu

Abstract
Discontinuous solid-solid phase transformations play a pivotal role in determining the properties of rechargeable battery electrodes. By leveraging *operando* Bragg Coherent Diffractive Imaging (BCDI), we investigate the discontinuous phase transformation in $Li_xNi_{0.5}Mn_{1.5}O_4$ within a fully operational battery. Throughout Li-intercalation, we directly observe the nucleation and growth of the Li-rich phase within the initially charged Li-poor phase in a 500 nm particle. Supported by the microelasticity model, the *operando* imaging unveils an evolution from a curved coherent to a planar semi-coherent interface driven by dislocation dynamics. We hypothesize these dislocations exhibit a glissile motion that facilitates interface migration without diffusion of host ions, leaving the particle defect-free post-transformation. Our data indicates negligible kinetic limitations from interface propagation impacting the transformation kinetics, even at a discharge rate of C/2. This study pioneers BCDI's capability to decode complex *operando* diffraction data, offering exciting opportunities to study nanoscale phase transformations with various stimuli.

Introduction
Over a century ago, Gibbs classified phase transformations into two fundamentally different types based on variations in the order parameter[1]. Continuous transformations exhibit variations that are "small in degree but may be great in its extent in space". The initial phase is unstable to infinitesimal fluctuations, resulting in a continuous change of the order parameter across large regions, which can be monitored by measuring macroscopic properties. For example, the order-disorder phase transformation in alloys is studied by measuring diffraction averaged over a large volume[2]. In contrast, discontinuous transformations display variations that are "initially smaller in extent but great in degree"[1]. An energy barrier stabilizes the system against infinitesimally small fluctuations until nucleation occurs at a localized region, causing a disruptive change in the order parameter. A classic example is the martensitic transformation in steel[3]. Capturing intermediate stages of a discontinuous phase transformation is significantly more challenging, as it requires time- and spatially resolved measurements to observe the nascent nucleus (often only a few nanometers large) and the subsequent interface propagation during growth. Yet, discontinuous phase transformations are of utmost importance in materials science because properties can be tuned by balancing nucleation and growth to achieve the desired microstructure[4,5].

X-ray powder diffraction proves to be a powerful tool for examining phase transformations with sufficient time resolution. During a phase transformation, the diffraction condition differs between

the coexisting phases, and each crystalline phase produces a distinct Debye-Scherrer ring[6–8]. Recent advances in high-brilliance synchrotron sources have enabled in-situ and *operando* measurements to capture diffraction signals from individual sub-micron particles[9]. In particular, Bragg Coherent Diffractive Imaging (BCDI) measures 3D strain distribution and buried defects within individual nanoparticles by inverting coherent diffraction data to real space structural information via an iterative phase retrieval algorithm[10–14]. In principle, BCDI offers an unparalleled opportunity to image nucleation and growth in individual particles under operating conditions, all without the need for specialized sampling environments. Nevertheless, the challenge of inverting complex diffraction data comprised of separated diffraction peaks has hindered the realization of real space imaging of discontinuous phase transformations with BCDI[15,16].

Here, we show BCDI's capability to image a discontinuous phase transformation induced by Li-intercalation in a single 500 nm large $Li_xNi_{0.5}Mn_{1.5}O_4$ ($0<x<1$) particle inside a fully operational battery. Like many high-rate cathode materials, the disordered spinel $Li_xNi_{0.5}Mn_{1.5}O_4$ experiences phase separation from the discontinuous phase transformation during cycling[17–20]. Through the transformation, internal stresses arise at the migrating interface that can impede kinetics and lead to mechanical degradations. Yet $Li_xNi_{0.5}Mn_{1.5}O_4$ shows great potential to outperform its commercial opponents in terms of stability and cost [22,23]. Using a newly developed correlated phase retrieval algorithm[16] to decode the phase-separating diffraction patterns, we directly observe the nucleation and growth of the Li-rich phase inside the initial, fully charged Li-poor phase. *Operando* imaging reveals the transformation of a curved coherent interface into a planar semi-coherent interface, driven by the introduction of dislocations. Supported by the microelasticity model, our data show that the dislocation array at the semi-coherent interface reorients the interface during operation. We see no evidence of kinetic limitation from the interface propagation on the phase transformation, even at a discharge rate of C/2 (full discharge in 2 hours). Our study unveils BCDI's potential as a robust tool for *operando* insights into discontinuous structural phase transformations in nanoscale systems, whether induced by electrochemical processes, temperature fluctuations, optical light exposure, or electronic excitation.

Results

Figure 1a shows the experimental setup for the *operando* measurements (figs. S1-2). During discharge, Li-ion intercalation induces a structural phase transformation from the Li-poor phase (smaller lattice constant, d_c) to the Li-rich phase (larger lattice constant, d_d)[6,20]. The different lattice spacing results in two separate Bragg reflections, $\mathbf{G}_{111,c}$ and $\mathbf{G}_{111,d}$. When the two phases coexist inside a single crystal, both Bragg reflections are present (Fig. 1b). The scattering amplitude is decorated by an interference pattern due to the illumination from spatially coherent x-rays on a single particle[10]. For a particle with coexisting phases, the superposition of the interference patterns captures the spatial distribution and the relative crystallographic registry of both phases, as well as the structure of the interface. To measure the 3D interference patterns, we recorded a series of 2D sections of the Ewald sphere across the reciprocal space by rocking the *operando* cell (fig. S3)[24].

Figure 1c-j presents the central slice of the measured *operando* 3D diffraction data as a function of depth of discharge (DoD, in equilibrium equivalent to x in $Li_xNi_{0.5}Mn_{1.5}O_4$) for the 111 Bragg peak of both phases (see fig. S4 for the full dataset with 50 measurements). At 0% DoD,

corresponding to the fully charged state, only one Bragg peak surrounded by interference fringes appears at the larger momentum transfer, Q_{111}, normal to the (111) planes (Fig. 1c). During the initial stages of discharge, spanning from 0% to 35% DoD, the main peak shows variations in its interference fringes suggesting local structural changes within the nanoparticle due to lithium intercalation (Fig. 1d and fig. S4). There is a slight decrease of the peak position along Q_{111}, indicating a solid solution behavior during the initial introduction of lithium[25]. Starting between 41.5% and 50.5% DoD (Fig. 1e-f), a secondary peak emerges around $Q_{111} = 1.34$ Å^{-1}, steadily gaining intensity at the cost of diminishing intensity in the primary peak (Fig. 1e-i). This is the hallmark of a discontinuous structural phase transformation, characterized by a substantial variation in the order parameter (namely, the lattice constant). The presence of both diffraction peaks emanating from an individual sub-micrometer crystal indicates phase coexistence. Notably, the presence of the coexisting peaks in the diffraction data occurs at the voltage plateau in the electrochemical data[26] (fig. S5), consistent with previous *operando* x-ray diffraction on $Li_xNi_{0.5}Mn_{1.5}O_4$ [6,12].

To interpret the measurements, we use the recently developed correlated phase retrieval algorithm[16] to invert the diffraction data into real-space 3D images. Critical for the success of the algorithm is inverting a series of *operando* measurements simultaneously, while assuming an approximately static shape of the particle across different discharge states (fig. S6). We argue that the assumption is true here because the material is stable for hundreds of charge-discharge cycles, suggesting retention of the particle shape during a single discharge. This assumption is also supported by the BCDI data on $Li_xNi_{0.5}Mn_{1.5}O_4$ before and after phase transformation[25]. The algorithm reconstructs the particle shape and the 3D displacement field along the scattering vector Q_{111}[12,13,27]. Subsequently, we derive the 3D strain distribution from this displacement field through numerical differentiation along Q_{111}[25]. The reconstructions are consistent across different runs (fig. S7) and the reconstructed diffraction patterns exhibit good agreement with the measured diffraction data (fig. S8), affirming the success of the phase retrieval procedure.

Figure 2 illustrates the *operando* strain evolution within a $Li_xNi_{0.5}Mn_{1.5}O_4$ nanoparticle, as obtained from the phase retrieval on the *operando* diffraction data (see figs. S9-10 for the full dataset of 50 images). Overall, the imaging data portrays the nucleation and growth of the Li-rich phase at the expense of the Li-poor phase through interface advancement (similar behavior is observed in another $Li_xNi_{0.5}Mn_{1.5}O_4$ particle, see figs. S11-12). At the onset of discharge, the nanoparticle consists of an almost homogeneous Li-poor phase (negative strain, depicted in blue) (Fig. 2a-c). As the electrochemical lithiation proceeds, an inclusion of the Li-rich phase (positive strain, depicted in red) nucleates at the bottom right corner of the nanoparticle (Fig. 2d). At this stage, the imaging suggests the presence of multiple nucleation sites (fig. S10); however, as the growth proceeds, only a single inclusion prevails (Fig. 2e). The merging is likely driven by surface tension, akin to Ostwald ripening or coarsening[28]. Throughout the subsequent lithiation, the Li-rich phase grows at the expense of the Li-poor phase via interface propagation (Fig. 2e-o). We approximate the interface propagation velocity to be 0.13 nm/s, notably slower than the expected Li-ions diffusion inside the particle (fig. S13). Consequently, the Li ions have sufficient time to equilibrate concentration gradients within each phase, likely resulting in a sharp Li-concentration gradient at the interface[29]. This is consistent with our observation that the interface width between the coexisting structures in Fig. 2i-j is less than 100 nm, approaching the spatial resolution of

operando BCDI[11,13]. By the end of the process, the nanoparticle is comprised entirely of the Li-rich phase (Fig. 2p).

In addition to visualizing in real time the nucleation and growth of a secondary phase, *operando* BCDI provides insights into the morphological evolution of the interface between the coexisting phases. Our data shows an initially curved interface (Fig. 2e-f) that subsequently transforms into a planar configuration (Fig. 2j-k, fig. S10). This morphological change is likely associated with the microstructure dynamics at the interface. Heterointerfaces between two distinct crystalline structural phases are typically classified into three types: coherent interfaces maintaining complete continuity of the lattice (Fig. 3a), semi-coherent interfaces with piecewise continuity separated by misfit dislocations (Fig. 3d), and incoherent interfaces with no registry between the two phases[30]. In our single-particle diffraction data, the coexisting phases generate diffraction peaks in proximity (less than 0.01Å^{-1} in $Q_\perp$ in Fig. 1e-h). Therefore, the two crystalline phases are closely aligned, ruling out a fully incoherent interface, which typically occurs when the crystal planes are misaligned by more than 15 degrees[31].

To distinguish between the coherent and semi-coherent heterointerface, we adopt the microelasticity model within the framework of continuum mechanics, which was adapted to study phase transformation in Li_xFePO_4 ($0<x<1$), another technically important phase separating cathode material[32,33]. For an inclusion of a secondary phase in a matrix, the strain energy is related to the function of direction, $B(\boldsymbol{n})$, which incorporates elastic properties of the system and crystallography of the phase transformation[34]. Minimization of the total strain energy requires aligning the interfaces of the inclusion with minima in $B(\boldsymbol{n})$. Here, we calculate $B(\boldsymbol{n})$ for an inclusion of the Li-rich phase inside the Li-poor phase (using Einstein notation for summation)

$$B(\boldsymbol{n}) = \lambda_{ijkl}\varepsilon^0_{ij}\varepsilon^0_{kl} - n_l\sigma^0_{ij}\Omega_{jl}(\boldsymbol{n})\sigma^0_{lm}\mathrm{n_m} \quad (1)$$

where $\boldsymbol{n}$ is the interface normal, ε^0_{ij} is the strain tensor, σ^0_{ij} is the stress tensor, Ω_{ij} is related to the elastic Green's tensor and defined as $\Omega^{-1}_{ij} = \lambda_{iklj}n_k n_l$, and λ_{ijkl} is the elastic stiffness tensor. Since the Li-poor phase transforms into the Li-rich phase while maintaining its cubic (spinel) symmetry[20], the transformation strain is isotropic and around 0.9% based on the difference in lattice parameters. The calculated $B(\boldsymbol{n})$ from equation (1) reveals a minimum direction along the family of <100> directions (Fig. 3b-c). Notably, the maximum direction of $B(\boldsymbol{n})$, <111>, differs from the minimum direction, <100>, by a mere 8%. Given this weak dependence of direction on $B(\boldsymbol{n})$, the modeling suggests an overall spherical shape of the interface, consistent with our observation in Fig. 2e-h.

As the structural transformation advances and the interfacial area expands, significant coherency strain arises[30,32]. To alleviate this strain, the interface can introduce misfit dislocations and form a semi-coherent interface (Fig. 3d). In this configuration, the interface comprises regions that maintain lattice continuity and is interspersed with dislocation cores that release interfacial strain and disrupt this continuity[30]. These misfit dislocations introduce an anisotropy to the transformation strain, consequently altering the orientations of the low-energy phase boundaries[32,33]. The transformation from coherent to semi-coherent interface here is reminiscent of the coherency loss in metals[35]. For the spinel structure, the slip directions and planes are $<110>$ and $\{111\}$[36]. We assume that the dislocations possess a Burgers vector along $[110]$ and lie within the $(\bar{1}11)$ plane (fig. S14). As a result, these dislocations lead to a loss of coherency along $[110]$. Setting $\varepsilon_{110} = 0$, the calculation shows the minimum $B(\boldsymbol{n})$ along $[\bar{1}10]$ (Fig. 3e), and the

difference between the lowest and highest $B(\boldsymbol{n})$ directions has increased to 197% (Fig. 3f). This strong anisotropy in $B(\boldsymbol{n})$ leads to a preferential interface orientation along $[\bar{1}10]$, and correspondingly, the microelasticity model predicts a transition of the interface geometry from a curved to a planar configuration, as we observe in Fig. 2h-i.

To validate the transition from a coherent to a semi-coherent interface, we examine the presence of dislocations at the interface after it transforms into the planar geometry. Dislocations manifest as singularities in the displacement field[12,13,27]. At the fully charged state (DoD = 1.2%), the particle exhibits uniform negative strain, and the displacement field is continuous without singularities (Fig. 4b). As the discharge progresses, the Li-rich phase with positive strain forms, leading to changes in the displacement field (Fig. 4c). At the interface, the continuity of the displacement field remains uninterrupted, showing no indications of structural defects such as dislocations. Yet, for the subsequent discharge, when the planar interface forms, the displacement map in Fig. 4d reveals an array of misfit dislocations. The presence of these dislocations corroborates our earlier hypothesis of a semi-coherent interface for strain relaxation in the microelasticity model. In this diffraction geometry, the phase discontinuity we measure is the projection of the Burgers vector along $[111]$. Our data is consistent with a Burgers vector along $[110]$ generating a phase discontinuity of 5.1 radians (fig. S15). Given a 0.9% lattice mismatch and the slip for each dislocation along the interface, we approximate one dislocation per 52 nm, which is of the same order of magnitude as the observed dislocation density of about one per 95 nm in Fig. 4d. The microelasticity model predicts an minimum-energy interface with a normal along $[\bar{1}10]$ (Figs. 3e,f), consistent with the strain map in Fig. 4d showing the interface orientation almost normal to the scattering vector Q_{111}.

Discussion

The access to crystal microstructure in our *operando* data provides insights into the nanomechanics at the propagating interface. The direction of dislocation motion has a significant component perpendicular to the Burgers vector. This motion is reminiscent of dislocation climb, a process requiring diffusion of host species (Ni, Mn, and O). Yet, $Li_xNi_{0.5}Mn_{1.5}O_4$ is reversible for hundreds of cycles[37], so a diffusional flux of host species during every cycle seems implausible. Drawing inspiration from the well-established theory of phase transformations in metals[30], we propose a model involving a glissile motion of interfacial dislocations. In this framework, the interface is generated through an invariant shear deformation and dislocations enter the crystal at the surface along the slip planes created by the shear (fig. S16)[31]. Thus, the interface can propagate conservatively without kinetically limited diffusion of host species[30]. As we see in the imaging of a $Li_xNi_{0.5}Mn_{1.5}O_4$ nanoparticle measured at a five times higher discharge rate, C/2, (fig. S17), phase separation is still evident in the strain maps despite that the two-phase reaction completes within 40 minutes (fig. S18). This suggests a transformation mechanism that is not limited by lithium diffusion but rather by the externally applied current that determines the discharge rate. Our results are consistent with recent phase-field modeling that suggests interfacial coherency loss can substantially improve reaction kinetics for high-rate cathode materials when the two-phase reaction is unavoidable[33]. When the phase transformation completes, the interfacial dislocations move along with the interface and exit the nanoparticle as Fig. 4e shows no dislocations.

Various models have been proposed to explain intercalation-driven phase transformations in rechargeable battery electrodes. Generally, ion transport inside the electrode and ion insertion kinetics across the electrode/electrolyte interface determine the phase transformation mechanism[29]. At fast (dis)charge rates (typically over 1C), the transformation kinetics is limited by ion diffusion, and a 'shrinking core' model was proposed to describe the phase separation during the transformation in Li_xFePO_4[38–40]. At slower (dis)charge rates (typically under 1C), the transformation kinetics is limited by the charge transfer across the surface of the electrode. Under this regime, models like the "domino-cascade" can explain the transformation of anisotropic ionic diffusion materials[41,42]. For isotropic diffusion materials such as $Li_xNi_{0.5}Mn_{1.5}O_4$, at discharge rates of C/2 and C/10, the 3D snapshots of our *operando* imaging reveal a nucleation and growth[43] transformation mechanism. Within this framework, the nucleus grows from a single localized point within the particle and extends through interface propagation. We directly observe transient misfit dislocations at the interface, which relax the large misfit strain of 0.9 % between the coexisting phases and likely prevent extensive cracking and fracture during the phase transformation. The speed of this transformation is controlled by the externally set discharge rate, free from intrinsic kinetic limitations due to the transient coherency loss at the interface.

Reflecting on Gibbs's classification, our research unveils BCDI as a powerful tool to study discontinuous phase transformations in *operando*. Moreover, the recently developed diffraction-limited synchrotron sources will boost BCDI's time resolution to seconds[44], enhancing our ability to observe these transformations at faster rates. Our results, therefore, unlock a feedback look between stimuli and characterization, which is critical for balancing the nucleation and growth in nanomaterials for optimizing materials' properties.

Materials and Methods

Sample synthesis and coin cell assembly

$Li_xNi_{0.5}Mn_{1.5}O_4$ disordered spinel was synthesized using the sol-gel method[45]. The coin cell was assembled using $Li_xNi_{0.5}Mn_{1.5}O_4$ as the cathode and Li metal as the anode (fig. S2). A 3 mm opening was created around the center of the base and top shells and sealed with a Kapton film to allow for X-ray transmission.

Bragg Coherent Diffractive Imaging experiment

The *operando* BCDI experiment was conducted at Sector 34-ID-C in the Advanced Photon Source at Argonne National Laboratory. A double crystal monochromator was used to select x-rays with energy of E = 9 keV. The coherent X-rays with a focus size of 800 nm were incident on a fully operational half-cell. The rocking curve around the 111 Bragg peak was collected by a 2D detector (Timepix, 256 × 256 pixels, each pixel 55μm × 55μm) around $2\theta = 17$ degrees ($\Delta\theta = \pm 0.3°$). The detector was placed 1.1 meter away from the sample and an evacuated flight tube was inserted between the sample and the detector. A total of 76 diffraction patterns were collected for a single 3D rocking scan with 1 second exposure time for each image. The 3D diffraction pattern of the same particle was continuously captured under *operando* conditions, while the coin cell battery was discharging. The low discharge rate was chosen to ensure that the particle remained around the same discharge state throughout one scan. Two discharge rates, C/10 and C/2, were chosen to illustrate the two-phase behavior under different rates. A C/10 rate indicates that the battery finishes discharge in 10 hours and a C/2 rate indicates that the battery finishes discharge in 2 hours. Each scan had a duration of about 2 minutes. Two rounds of alignment scans in the labx, labz (sample position relative to the incident beam) and theta directions were taken between every three rocking scans to ensure that the particle did not move out of the beam or rotate away from the diffraction condition.

Phase retrieval

The details of the correlated data inversion algorithm were reported elsewhere[16]. Here, for brevity we summarize the main aspects of the algorithm we used to invert the *operando* data. 10 diffraction scans that describe the entire two-phase reaction were inverted simultaneously. Every diffraction scan was aligned such that the center of each diffraction had the same scattering vector (during the experiment, the scattering angle was shifted to follow the peak evolution). The data inversion started with each scan running 30 reconstructions individually, each initiated with a random phase. For every 10 iterations, the error matrix of the correlation within the 30 reconstructions was calculated for each scan. Then we averaged the support of the 5 best-correlated reconstructions in each scan across all 10 scans (in total 50 reconstructions) while leaving the displacement fields unchanged. Then the averaged support was multiplied by the individual support and became the input support for the next set of reconstructions. The reconstruction consisted of a total of 610 iterations with alternating 10 iterations of the ER algorithm and 50 iterations of the RAAR algorithm. For the primary particle in the main text, five datasets that contain mutually different scans were reconstructed and then stitched back together into a single sequence. The series shown in Fig. 2 and Fig. S8 is a collage of multiple independent reconstruction procedures, i.e, some have no overlap of the diffraction data taken for the reconstructions. We take the continuous evolution of the nucleation and growth as a testament for the robustness of the algorithm. For the supplementary particle, one dataset that consists of 13 scans and one dataset that consists of 15 scans were reconstructed. The algorithm

was performed 10 times on each dataset and the final imaging is the result of 5 × 10 reconstructions of each scan.

Acknowledgements

The work at Cornell was supported by the National Science Foundation under award number CAREER DMR-1944907. The work at UC San Diego was supported by the Sustainable Power and Energy Center (SPEC) and US Department of Energy, Office of Science, Office of Basic Energy Sciences, under contract No. DE-SC0001805. This research used resources of the Advanced Photon Source, a U.S. Department of Energy (DOE) Office of Science user facility operated for the DOE Office of Science by Argonne National Laboratory under Contract No. DE-AC02-06CH11357.

References

1. Gibbs, J. W. *On the Equilibrium of Heterogeneous Substances*. vol. 2 300–320 https://archiv.ub.uni-heidelberg.de/volltextserver/13220/ (1879).
2. Darul, J., Nowicki, W., Piszora, P., Baehtz, C. & Wolska, E. Synchrotron X-ray powder diffraction studies on the order–disorder phase transition in lithium ferrites. *Journal of Alloys and Compounds* **401**, 60–63 (2005).
3. Krauss, G. Martensite in steel: strength and structure. *Materials Science and Engineering: A* **273–275**, 40–57 (1999).
4. Easterling, D. A. P., Kenneth E. Easterling, Kenneth E. *Phase Transformations in Metals and Alloys (Revised Reprint)*. (CRC Press, Boca Raton, 2009). doi:10.1201/9781439883570.
5. Wilde, G. Structural Phase Transformations in Nanoscale Systems. *Advanced Engineering Materials* **23**, 2001387 (2021).
6. Singer, A. *et al.* Nonequilibrium structural dynamics of nanoparticles in LiNi1/2Mn3/2O4 cathode under operando conditions. *Nano Letters* **14**, 5295–5300 (2014).
7. Huang, J. J. *et al.* Disorder Dynamics in Battery Nanoparticles During Phase Transitions Revealed by Operando Single-Particle Diffraction. *Advanced Energy Materials* **12**, 2103521 (2022).
8. Liu, H. *et al.* Capturing metastable structures during high-rate cycling of LiFePO4 nanoparticle electrodes. *Science* **344**, 1252817 (2014).
9. Lin, F. *et al.* Synchrotron X-ray Analytical Techniques for Studying Materials Electrochemistry in Rechargeable Batteries. *Chem. Rev.* **117**, 13123–13186 (2017).
10. Robinson, I. & Harder, R. Coherent X-ray diffraction imaging of strain at the nanoscale. *Nature Mater* **8**, 291–298 (2009).

11. Clark, J. N. *et al.* Three-dimensional imaging of dislocation propagation during crystal growth and dissolution. *Nature Materials* **14**, 780–784 (2015).
12. Ulvestad, U. *et al.* Topological defect dynamics in operando battery nanoparticles. *Science* **348**, 1344–1347 (2015).
13. Singer, A. *et al.* Nucleation of dislocations and their dynamics in layered oxide cathode materials during battery charging. *Nature Energy* **3**, 641–647 (2018).
14. Pfeifer, M. A., Williams, G. J., Vartanyants, I. A., Harder, R. & Robinson, I. K. Three-dimensional mapping of a deformation field inside a nanocrystal. *Nature* **442**, 63–66 (2006).
15. Diao, J. *et al.* Evolution of ferroelastic domain walls during phase transitions in barium titanate nanoparticles. *Phys. Rev. Materials* **4**, 106001 (2020).
16. Wang, Z., Gorobtsov, O. & Singer, A. An algorithm for Bragg coherent x-ray diffractive imaging of highly strained nanocrystals. *New Journal of Physics* **22**, (2020).
17. Sharma, N. *et al.* Direct Evidence of Concurrent Solid-Solution and Two-Phase Reactions and the Nonequilibrium Structural Evolution of LiFePO4. *Journal of the American Chemical Society* **134**, (2012).
18. Wagemaker, M. *et al.* A Kinetic Two-Phase and Equilibrium Solid Solution in Spinel Li4+xTi5O12. *Advanced Materials* **18**, 3169–3173 (2006).
19. Ganapathy, S., Vasileiadis, A., Heringa, J. R. & Wagemaker, M. The Fine Line between a Two-Phase and Solid-Solution Phase Transformation and Highly Mobile Phase Interfaces in Spinel Li4+xTi5O12. *Advanced Energy Materials* **7**, (2017).
20. Kim, J.-H., Yoon, C. S., Myung, S.-T., Prakash, J. & Sun, Y.-K. Phase Transitions in Li1 − δ Ni0.5Mn1.5 O 4 during Cycling at 5 V. *Electrochem. Solid-State Lett.* **7**, A216 (2004).

21. Mariyappan, S., Wang, Q. & Tarascon, J. M. Will Sodium Layered Oxides Ever Be Competitive for Sodium Ion Battery Applications? *J. Electrochem. Soc.* **165**, A3714 (2018).
22. Liang, G., Peterson, V. K., See, K. W., Guo, Z. & Kong Pang, W. Developing high-voltage spinel LiNi 0.5 Mn 1.5 O 4 cathodes for high-energy-density lithium-ion batteries: current achievements and future prospects. *Journal of Materials Chemistry A* **8**, 15373–15398 (2020).
23. Zhao, H. *et al.* Cobalt-Free Cathode Materials: Families and their Prospects. *Advanced Energy Materials* **12**, 2103894 (2022).
24. Williams, G. J., Pfeifer, M. A., Vartanyants, I. A. & Robinson, I. K. Three-Dimensional Imaging of Microstructure in Au Nanocrystals. *Physical Review Letters* **90**, 4 (2003).
25. Ulvestad, A. *et al.* Single particle nanomechanics in operando batteries via lensless strain mapping. *Nano Letters* **14**, 5123–5127 (2014).
26. Van der Ven, A., Bhattacharya, J. & Belak, A. A. Understanding Li Diffusion in Li-Intercalation Compounds. *Acc. Chem. Res.* **46**, 1216–1225 (2013).
27. Sun, Y. *et al.* X-ray Nanoimaging of Crystal Defects in Single Grains of Solid-State Electrolyte Li7-3 xAlxLa3Zr2O12. *Nano Letters* **21**, 4570–4576 (2021).
28. Sethna, J. P. *Entropy, Order Parameters, and Complexity*. (Oxford University Press, 2022).
29. Singh, G. K., Ceder, G. & Bazant, M. Z. Intercalation dynamics in rechargeable battery materials: General theory and phase-transformation waves in LiFePO4. *Electrochimica Acta* **53**, 7599–7613 (2008).
30. Sutton, A. P. & Balluffi, R. W. *Interfaces in Crystalline Materials*. (Oxford University Press, Oxford, New York, 2007).

31. Balluffi, R. W., Allen, S. M. & Carter, W. C. *Kinetics of Materials*. (John Wiley & Sons, 2005).
32. Cogswell, D. A. & Bazant, M. Z. Coherency strain and the kinetics of phase separation in LiFePO 4 nanoparticles. *ACS Nano* **6**, 2215–2225 (2012).
33. Heo, T. W., Tang, M., Chen, L.-Q. & Wood, B. C. Defects, Entropy, and the Stabilization of Alternative Phase Boundary Orientations in Battery Electrode Particles. *Advanced Energy Materials* **6**, 1501759 (2016).
34. Khachaturyan, A. G. *Theory of Structural Transformations in Solids*. (Courier Corporation, 2013).
35. Shi, R., Ma, N. & Wang, Y. Predicting equilibrium shape of precipitates as function of coherency state. *Acta Materialia* **60**, 4172–4184 (2012).
36. Callister, W. D. *Fundamentals of Materials Science and Engineering: An Integrated Approach*. (John Wiley & Sons, cop., Hoboken, N.J., 2013).
37. Cho, H.-M., Chen, M. V., MacRae, A. C. & Meng, Y. S. Effect of Surface Modification on Nano-Structured LiNi0.5Mn1.5O4 Spinel Materials. *ACS Appl. Mater. Interfaces* **7**, 16231–16239 (2015).
38. Padhi, A. K., Nanjundaswamy, K. S. & Goodenough, J. B. Phospho-olivines as Positive-Electrode Materials for Rechargeable Lithium Batteries. *J. Electrochem. Soc.* **144**, 1188 (1997).
39. Andersson, A. S., Kalska, B., Häggström, L. & Thomas, J. O. Lithium extraction/insertion in LiFePO4: an X-ray diffraction and Mössbauer spectroscopy study. *Solid State Ionics* **130**, 41–52 (2000).

40. Srinivasan, V. & Newman, J. Discharge Model for the Lithium Iron-Phosphate Electrode. *J. Electrochem. Soc.* **151**, A1517 (2004).
41. Delmas, C., Maccario, M., Croguennec, L., Le Cras, F. & Weill, F. Lithium deintercalation in LiFePO4 nanoparticles via a domino-cascade model. *Nature Materials 2008 7:8* **7**, 665–671 (2008).
42. Bazant, M. Z. Theory of Chemical Kinetics and Charge Transfer based on Nonequilibrium Thermodynamics. *Acc. Chem. Res.* **46**, 1144–1160 (2013).
43. Kuppan, S., Xu, Y., Liu, Y. & Chen, G. Phase transformation mechanism in lithium manganese nickel oxide revealed by single-crystal hard X-ray microscopy. *Nature Communications* **8**, (2017).
44. Raimondi, P. ESRF-EBS: The Extremely Brilliant Source Project. *Synchrotron Radiation News* **29**, 8–15 (2016).
45. Cho, H.-M. & Meng, Y. S. Effect of Ni/Mn Ordering on Elementary Polarizations of LiNi0.5Mn1.5O4 Spinel and Its Nanostructured Electrode. *J. Electrochem. Soc.* **160**, A1482 (2013).

Figures

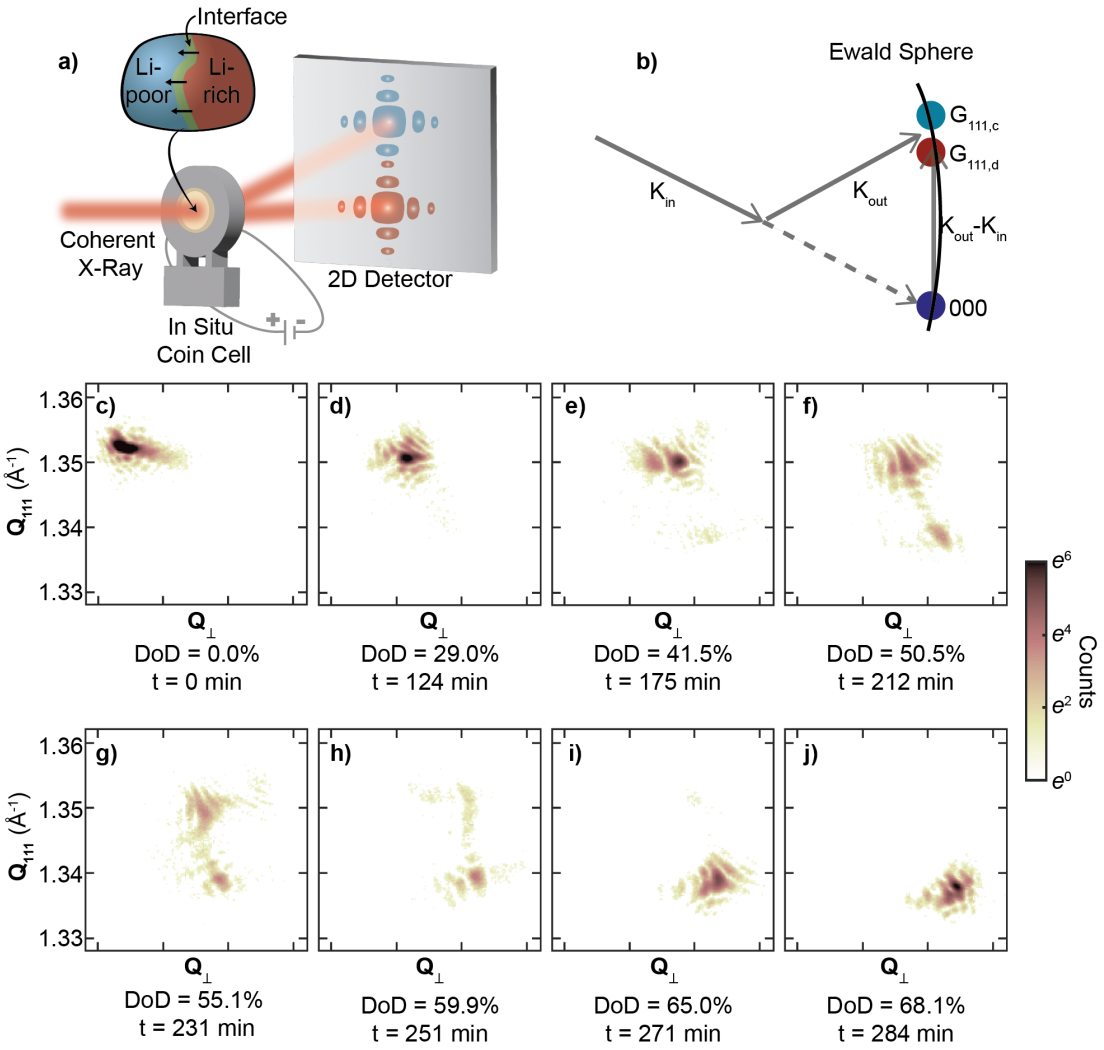

Figure 1. Operando Bragg Coherent Diffraction of a single $Li_xNi_{0.5}Mn_{1.5}O_4$ nanoparticle during the discontinuous solid-solid phase transformation induced by electrochemical Li-insertion. a) Experimental setup showing the operando coin cell, illuminated by coherent X-rays at 9 keV with a focus size of 800 nm, and diffraction around the 111 Bragg peak recorded on an area detector. During discharge, the $Li_xNi_{0.5}Mn_{1.5}O_4$ particle undergoes a discontinuous phase transformation via phase coexistence of the Li-poor phase (in blue) and Li-rich phase (in red), separated by the interface (in green). **b**) Schematic illustrating the Ewald sphere construction mapping out the interference profile surrounding the reciprocal lattice points $G_{111,d}$ (Li-rich phase) and $G_{111,c}$ (Li-poor phase). The area detector records a segment of the Ewald sphere. As it intersects both reciprocal space vectors, the detector image shows a split peak. **c**) – **j**) Cross-sections of the 3D diffraction pattern for the same $Li_xNi_{0.5}Mn_{1.5}O_4$ nanoparticle at various depths of discharge. The depth of discharge (DoD) is defined as the fraction of the capacity that is currently removed from its full capacity. The vertical axis shows the lattice spacing, d, determined as $2\pi/q$, where q is the coordinate in reciprocal space.

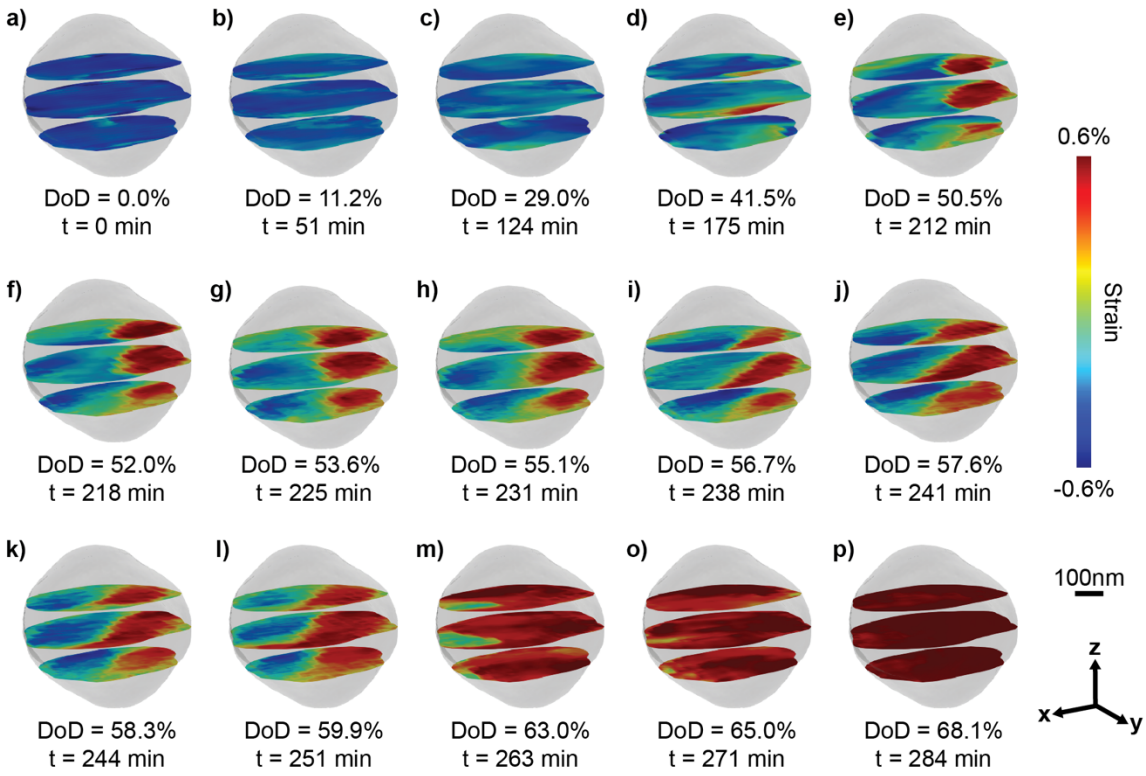

Figure 2. Operando visualization of the coexisting phases during the structural phase transformation under lithium intercalation. a) – p) The 3D strain field inside a single $Li_xNi_{0.5}Mn_{1.5}O_4$ nanoparticle during the two-phase reaction induced by Li intercalation. The strain maps are extracted by inverting coherent x-ray diffraction data shown in Figure 1 c-j and Fig.S4. The semi-transparent isosurface portrays the particle shape, while the colored slices display the strain distribution, $\varepsilon_{111}(\boldsymbol{r})$, illustrated on three chosen planes. We show the strain field, $\varepsilon_{111}(\boldsymbol{r})$, as the local lattice constant compared to the average lattice constant, d_a, of the (111) planes between the fully charged, Li-poor (d_c) and the partially discharged, Li-rich (d_d) phase, where $d_a = (d_c + d_c)/2$ and $\varepsilon_{111}(r) = d(r)/d_a - 1$. At 0% DoD in **a)**, the particle has a uniform negative strain shown in blue, corresponding to the Li-poor phase with a small lattice constant, d_c. At the end of the two-phase reaction around 68.1% DoD in **p)**, the particle presents a uniform positive strain shown in red, corresponding to the Li-rich phase with a large lattice constant d_d. Q_{111} points along z.

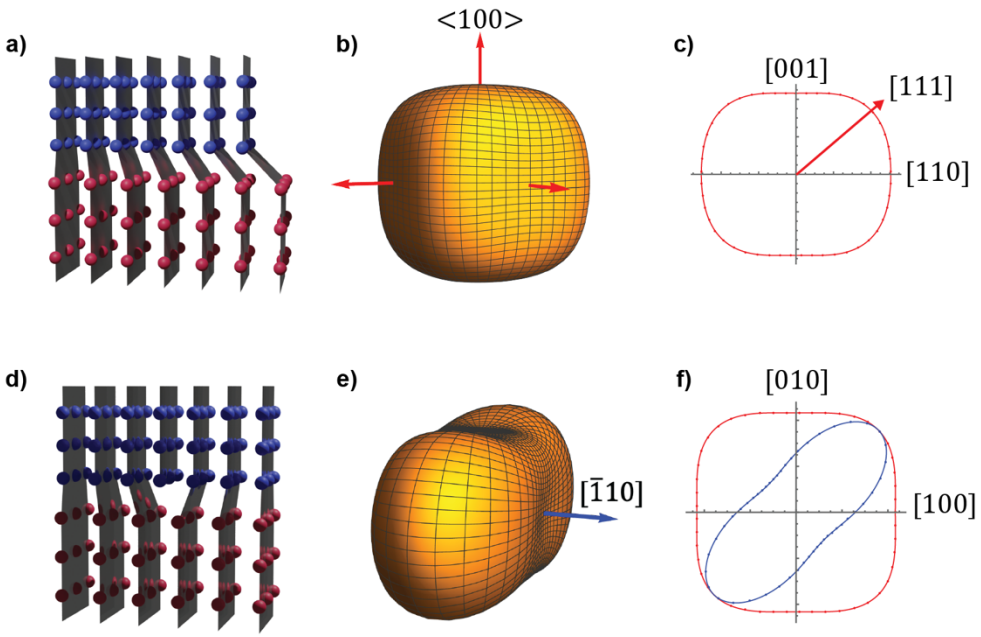

Figure 3. Microelasticity theory for coherent and semi-coherent interface in $Li_xNi_{0.5}Mn_{1.5}O_4$. a) Illustration showing a coherent interface. Each plane of blue atoms representing the Li-poor phase is connected to a plane of the red atoms representing the Li-rich phase. The lattice distortion gradually intensifies from the left to the right. **b)** Isosurface plot of the elastic strain energy as a function of normal direction for a coherent interface. The red arrows indicate the energy minima directions, <100>. **c)** 2D parametric plot of the strain energy illustrated in **b)** in the plane spanning the [001] and [110] directions. The energy minimum, [001], and maximum direction, [111], display similar values. **d)** Illustration of a semi-coherent interface with a misfit edge dislocation – one extra half-plane inserted from the top – that relieves the misfit strain in the direction of the Burgers vector perpendicular to the half-plane. **e)** Isosurface plot of elastic strain energy for a semi-coherent interface with coherency loss in the [110] direction. The blue arrow indicates the energy minimum direction along [$\bar{1}$10]. **f)** 2D parametric plot in the plane spanning [100] and [010], comparing strain energy between a coherent (red) and a semi-coherent (blue) interface. The semi-coherent interface exhibits significant anisotropy in its strain energy.

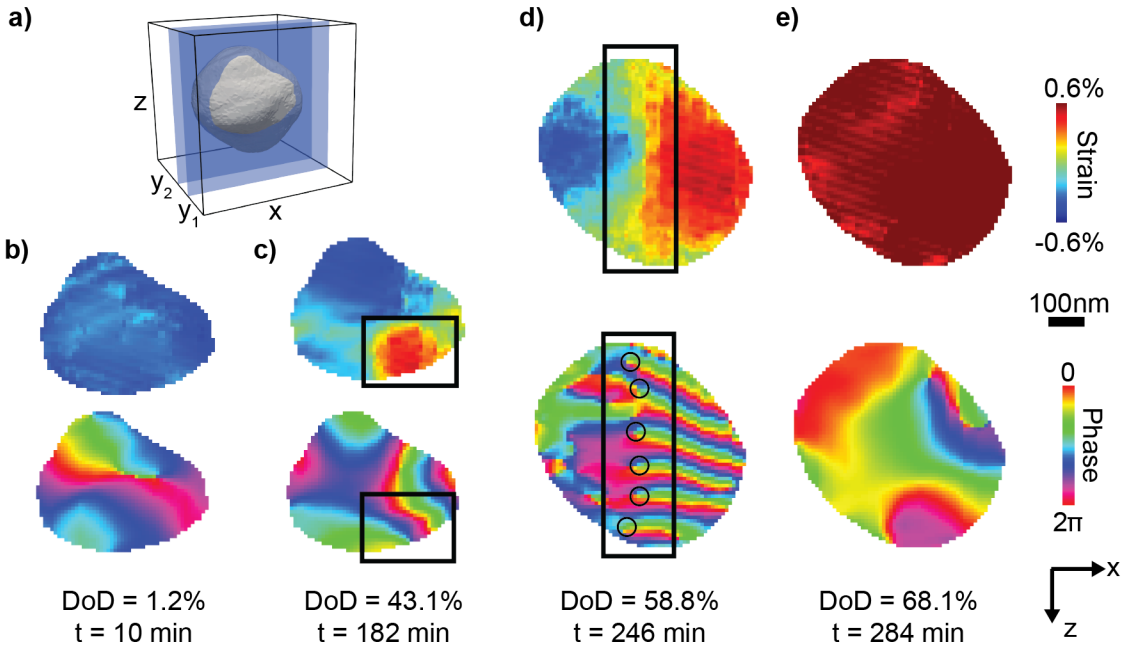

Figure 4. The cross-sections of the reconstructed strain and displacement field in the *xz* plane at different depths of discharge. a) Three-dimensional representation of the LNMO particle aligned at the same angle as in Figure 2 but with two slices taken along a different direction. **b) – e)** Reconstructed strain (top) and lattice displacement (bottom) maps. **b)** Prior to the phase transformation, the strain map corresponds to a fully charged Li-poor phase. The false color in the phase maps reflects the displacement from the ideal lattice at each position. **c)** At the early stage of the phase transformation, the Li-rich phase (enclosed by the rectangle) nucleates at the lower right corner, leading to an intensified color gradient within the rectangle. Both *xz* slices in **b)** and **c)** are located at y_1 in **a)**, 170 nm away from the center of the particle where the discharged phase starts to nucleate. **d)** During the phase transformation, the nucleated Li-rich phase forms a semi-coherent interface with the Li-poor phase (outlined by the rectangle), which contains an array of dislocations each denoted by ⊥ in the phase map. The dislocations run into the page and propagate along the negative x-direction with the interface. **e)** At the end of phase transformation, the strain map shows the Li-rich phase with no observable signs of dislocations in the phase map. The *xz* slices in **d)** and **e)** are located at y_2 in **a)**, at the center of the particle. The scattering vector, **Q**, points along the *z*-axis.

Operando real-space imaging of a structural phase transformation in a high-voltage electrode: Supplementary Information

Yifei Sun[1], Sunny Hy[2], Nelson Hua[3,4], James Wingert[3], Ross Harder[5], Ying Shirley Meng[2,6], Oleg Shpyrko[3], Andrej Singer[1,]*

[1]*Department of Materials Science and Engineering, Cornell University, Ithaca, New York 14850, USA*
[2]*Department of Nanoengineering, University of California San Diego, La Jolla, California, 92093, USA*
[3]*Department of Physics, University of California San Diego, La Jolla, California, 92093, USA*
[4]*Laboratory for X-ray Nanoscience and Technologies, Paul Scherrer Institut, 5232 Villigen, Switzerland*
[5]*Advanced Photon Source, Argonne National Laboratory, Argonne, Illinois, 60439, USA*
[6]*Pritzker School of Molecular Engineering, University of Chicago, Chicago, Illinois, 60637, USA*
[*]asinger@cornell.edu

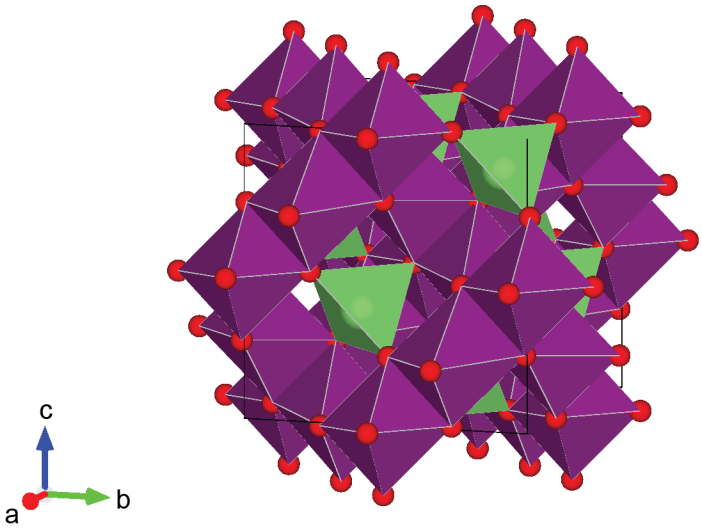

Fig. S1. Crystal structure of the disordered $Li_xNi_{0.5}Mn_{1.5}O_4$. The disordered $Li_xNi_{0.5}Mn_{1.5}O_4$ has the cubic spinel structure with the space group $Fd\bar{3}m$. The Ni and Mn reside within the purple octahedra with Ni occupying 25% of the sites and Mn occupying 75% of the sites randomly. The Li resides within the green tetrahedra. The red atoms are oxygens.

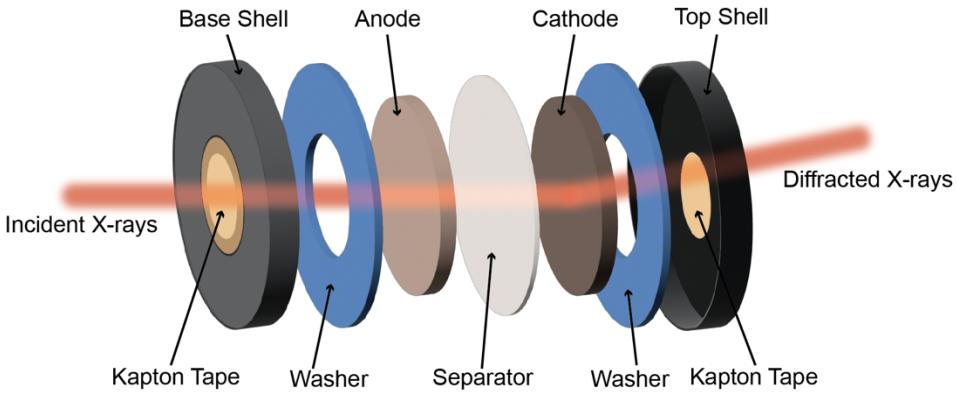

Fig. S2. Expanded view of the operando coin cell. The cell top and base are from the standard CR2032 cells, which have a diameter of 20 mm and a height of 3.2 mm. Both sides have a hole drilled at the center of size around 3 mm in diameter, which is sealed by Kapton tape. The cell is placed so that the material of interest, the $Li_xNi_{0.5}Mn_{1.5}O_4$ cathode nanoparticles, is located downstream from the incident X-rays. The anode is lithium metal, and the separator (Celgard C480) contains electrolyte of 1 M solution of lithium hexafluorophosphate ($LiPF_6$) in a 1:1 volume mixture of ethylene carbonate (EC) and dimethyl carbonate (DMC).

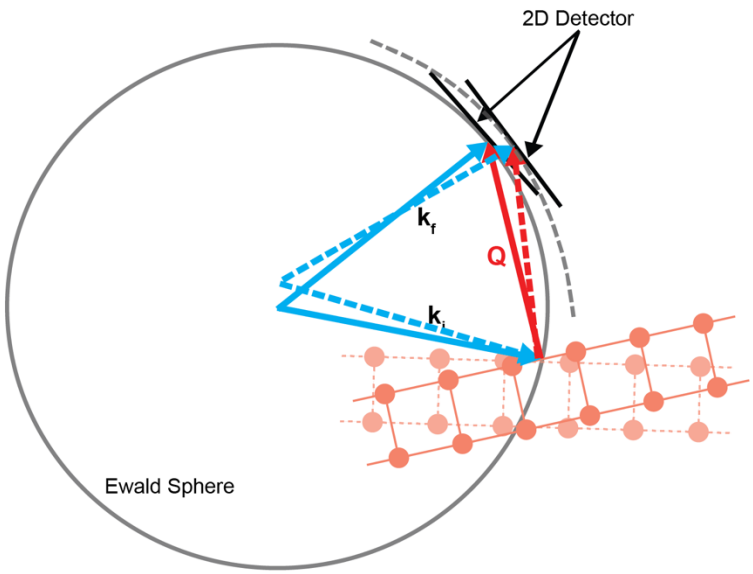

Fig. S3. Ewald sphere construction. Rocking the crystal, shown as lattice plane in red, results in the Ewald sphere slicing the vicinity of the Bragg peaks at different positions in the reciprocal space. This is equivalent to shifting the detector perpendicular to the Ewald sphere around the Bragg peaks. The nearly parallel slices were combined to obtain a 3D pattern[1].

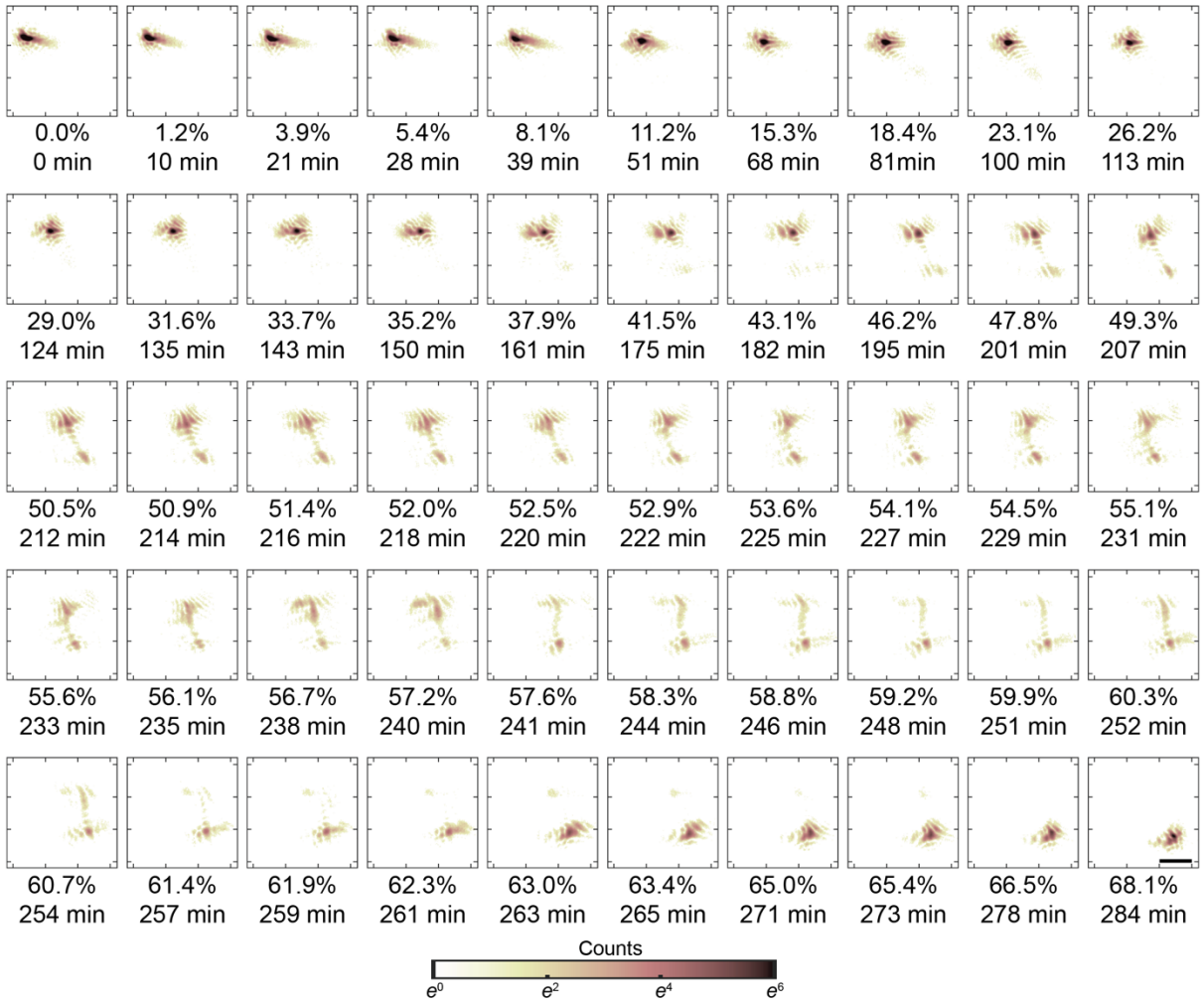

Fig. S4. Full set of the operando diffraction data from a single $Li_xNi_{0.5}Mn_{1.5}O_4$ particle undergoing a structural phase transformation during discharge. Diffraction data shows the decrease of intensity of the lithium-poor phase (larger Q) and the increase of intensity of the lithium-rich phase (smaller Q). During the transition, two peaks coexist, indicating the presence of both phases inside the $Li_xNi_{0.5}Mn_{1.5}O_4$ nanoparticle. The two-phase reaction ends around when the battery is 68% discharged. The scalebar is 0.1 nm^{-1}. The diffraction data is inverted using the correlated phase retrieval algorithm.

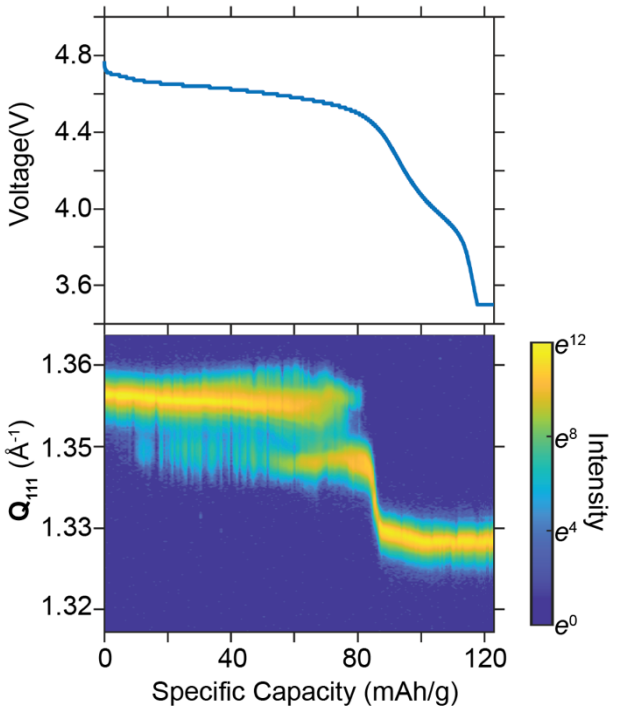

Fig. S5. Electrochemical data of the cell (top) and diffraction data of a single $Li_xNi_{0.5}Mn_{1.5}O_4$ particle within the cell (bottom). The voltage plateau in the electrochemical data coincides with the two-peak coexistence region in the diffraction data. This indicates that the electrochemistry behavior of the $Li_xNi_{0.5}Mn_{1.5}O_4$ particle that we selected for reconstruction is representative for all active material. When the specific capacity reaches around 80 mAh/g, the cell enters the solid-solution regime, which is reflected as one diffraction peak continuously shifting its Q position.

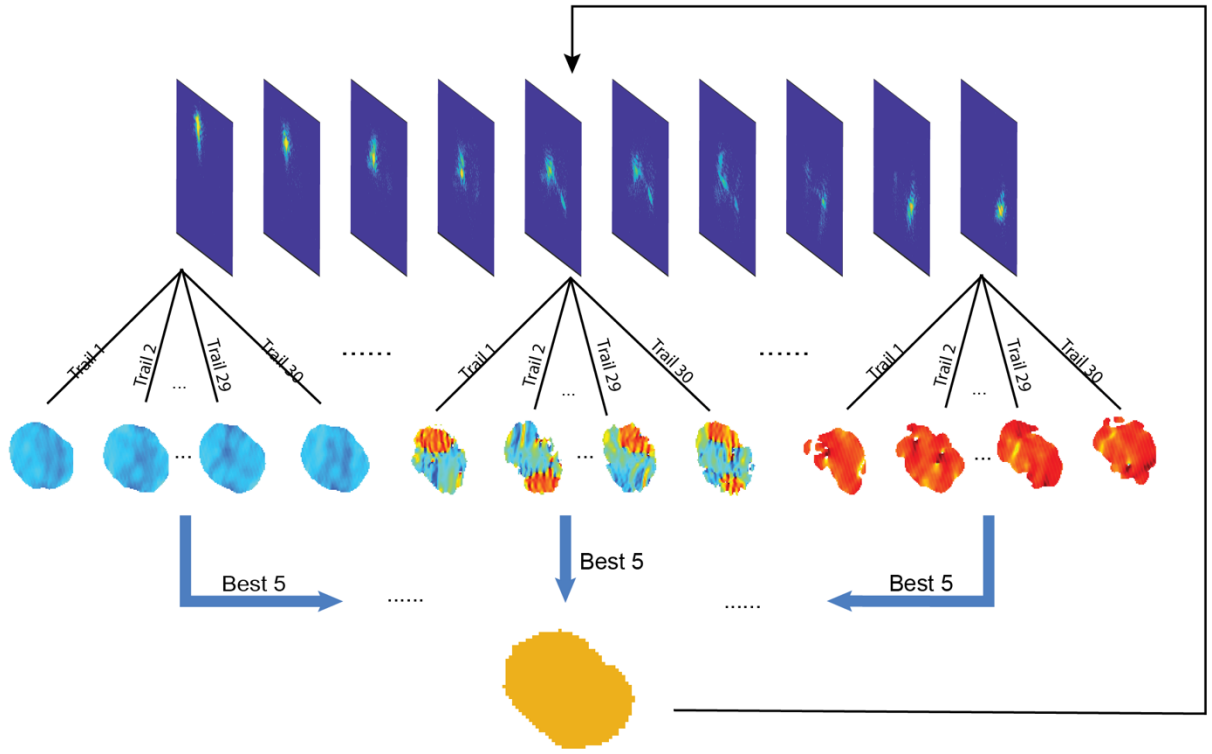

Fig. S6. Illustration of the correlated phase retrieval algorithm. The illustration shows one iteration of the algorithm. A set of scans (we used 10 scans) that include both single-peak and two-peak diffraction are reconstructed with alternating Error Reduction (ER)[2] and Relaxed Averaged Alternating Reflections (RAAR)[3] phase retrieval algorithms separately 30 times. Each individual reconstruction is called a trail. Out of the 30 trails for each scan, we select the best 5 trails. The support of the reconstruction for next iteration is then calculated by averaging the shape of the best 5 trails for all 10 scans. During the selection of the best 5 trails, the particle shape can appear inverted (two solutions, $S(\boldsymbol{r})$ and $S^*(-\boldsymbol{r})$, are indistinguishable, where $\boldsymbol{r}$ is the coordinate and * denotes complex conjugate). To determine if the reconstruction is inverted, we cross-correlate strain among different reconstructions.

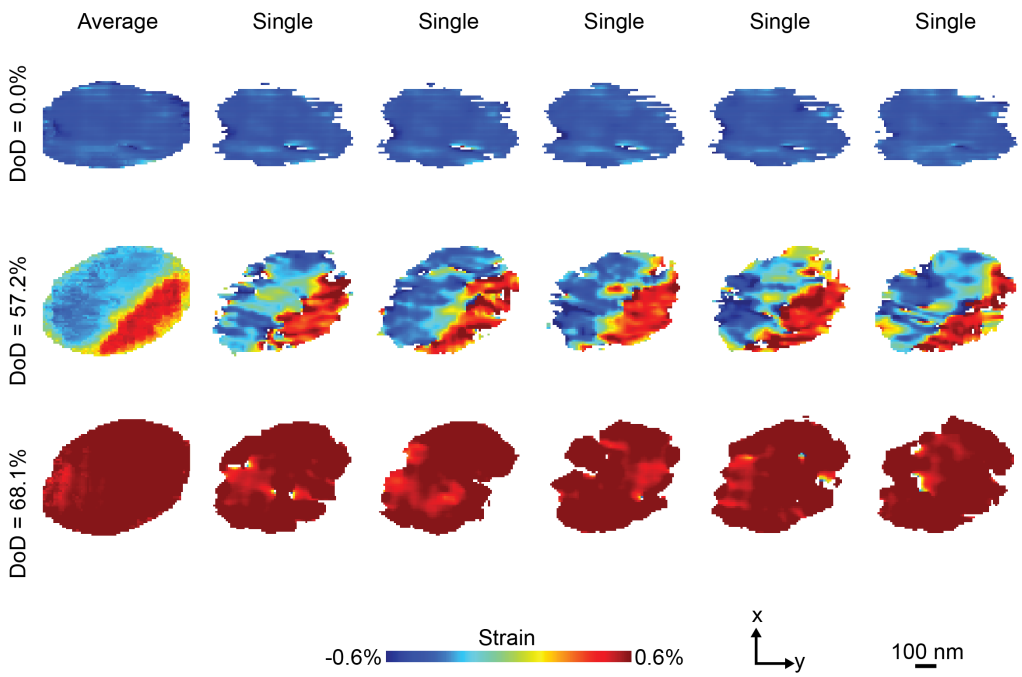

Fig. S7. Comparison of strain between separate reconstructions and the average result. Each single reconstruction starts with a different random start. Strain is then calculated by taking the derivative of the reconstructed displacement field along the scattering vector Q. The average strain is taken from averaging individual strains of 50 reconstructions, each with a different random start. At different depths of discharge, 0%, 57.2%, and 68.1%, the strain of single reconstructions is consistent with each other, and the average strain is representative of the single strains.

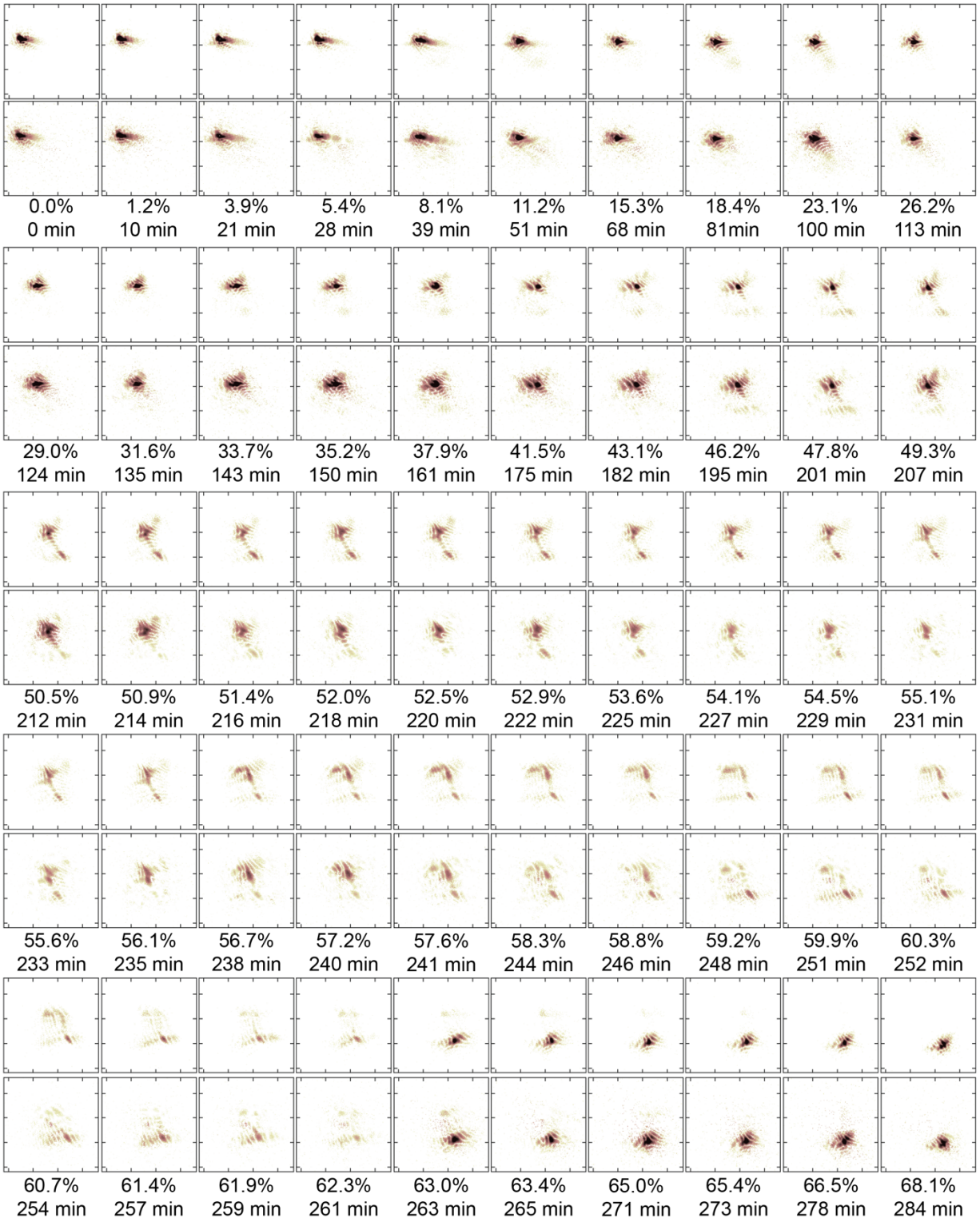

Fig. S8. A side-by-side comparison of the central theta slice from the measured diffraction (top) and the Fourier transform of reconstructions (bottom). The close alignment between the reconstructed results and the diffraction data is indicative of successful phase retrieval. The false colors are identical to Fig. S4.

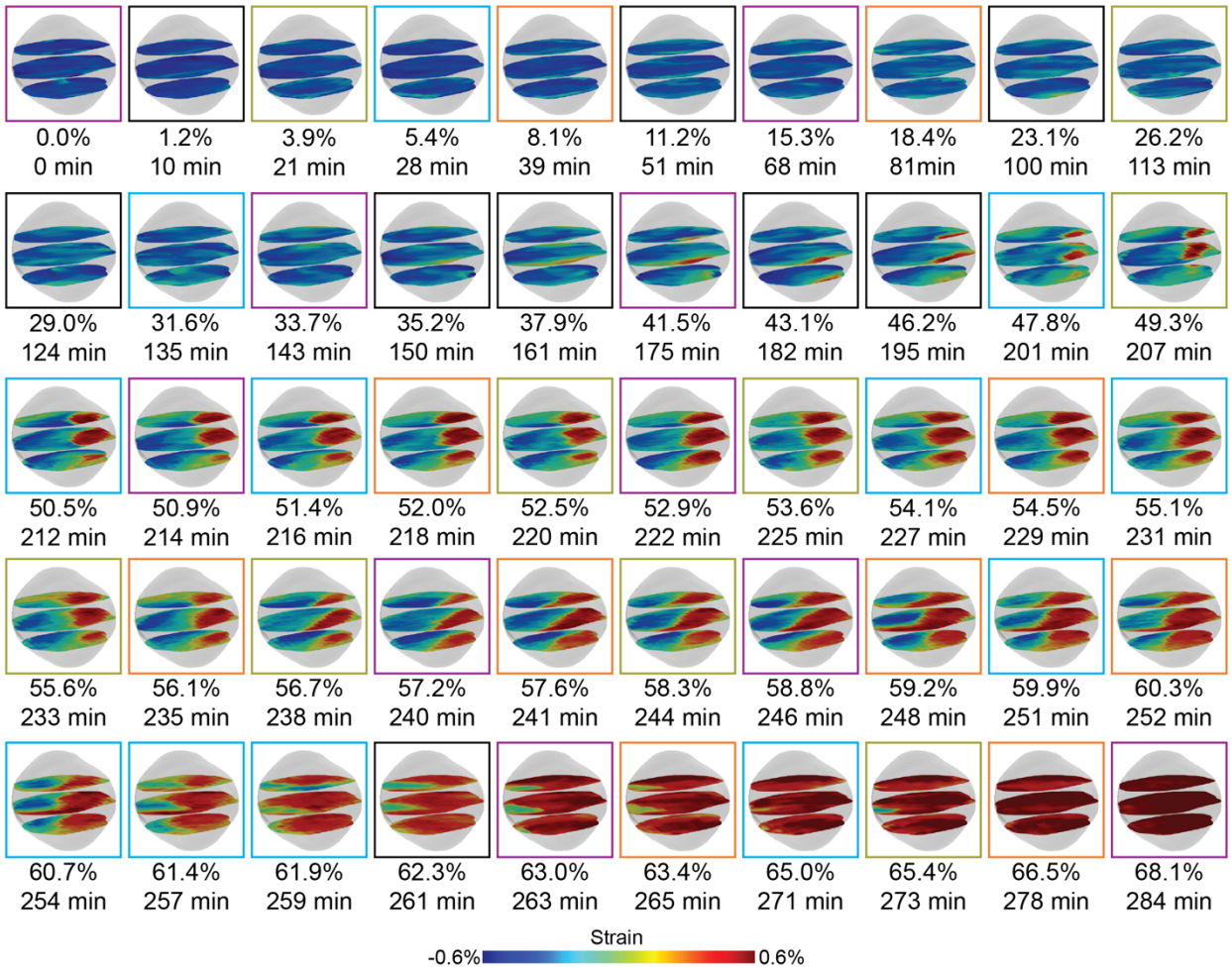

Fig. S9. Full set of the operando imaging of the structural phase transformation during discharge. For each depth of discharge, the chosen planes at the same position are imaged for the visualization of strain distribution inside the entire particle. The color of the box around each image highlights different reconstruction runs. The particle starts with a uniform negative strain (Li-poor phase) and ends the two-phase reaction with a uniform positive strain (Li-rich phase). The intermediate stages show that particle has both the red and blue phases, where the red phase grows at the expanse of blue phase, defining a nucleation and growth mechanism for the two-phase reaction. The particle is about 500 nm large.

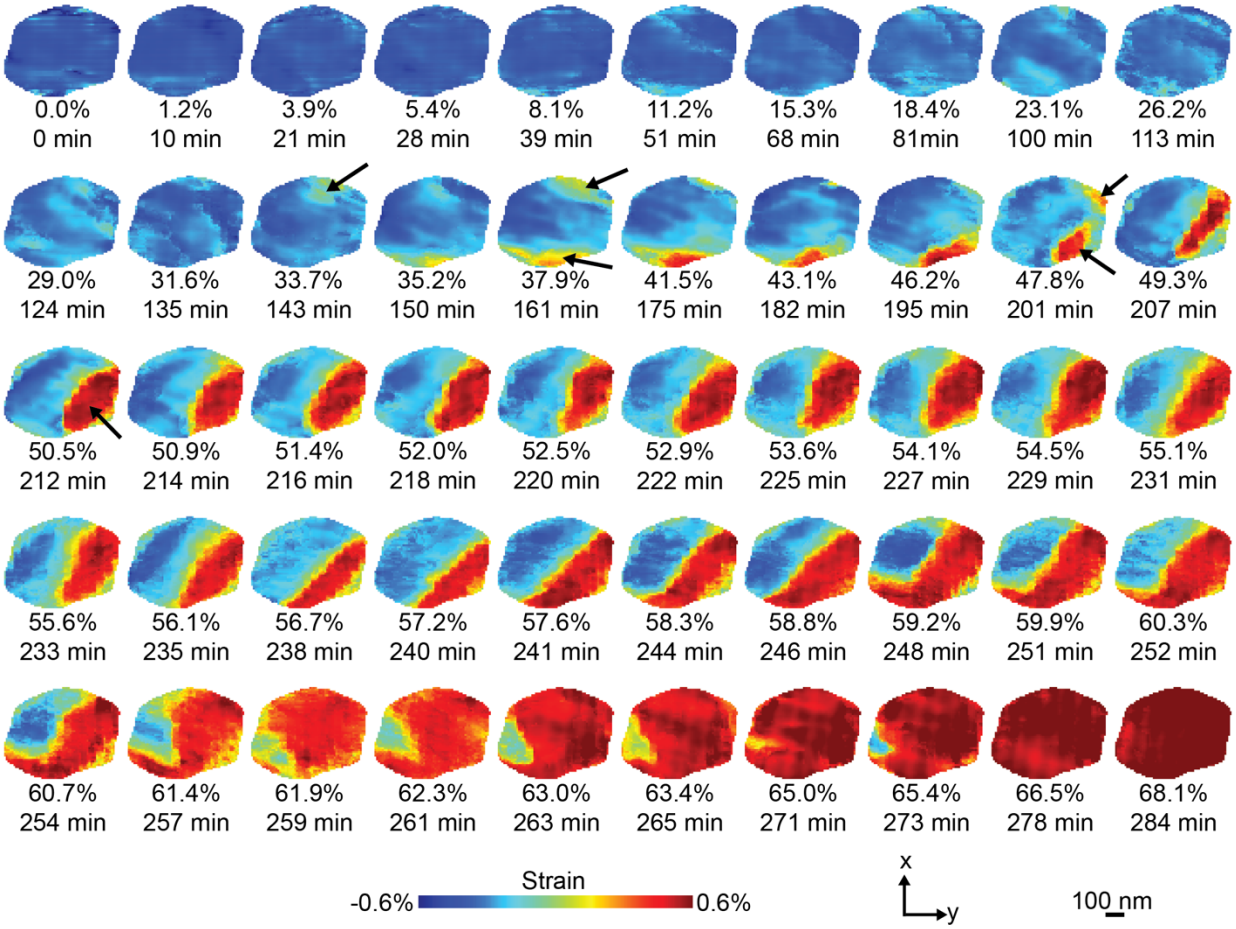

Fig. S10. 2D view of the central slice in Fig. S9. The arrows indicate the nucleation sites of the new Li-rich phase (red) inside the Li-poor phase (blue). When the Li-rich phase nucleates, it starts around the edge of the particle and can occur simultaneously at multiple locations (DoD = 37.9%). As the Li-rich phase continues to grow, the nucleated sites grow and, in the meantime, coalesce (DoD =47.8%). Later, the nucleated sites merge for a total reduction of interface area (DoD = 50.5%).

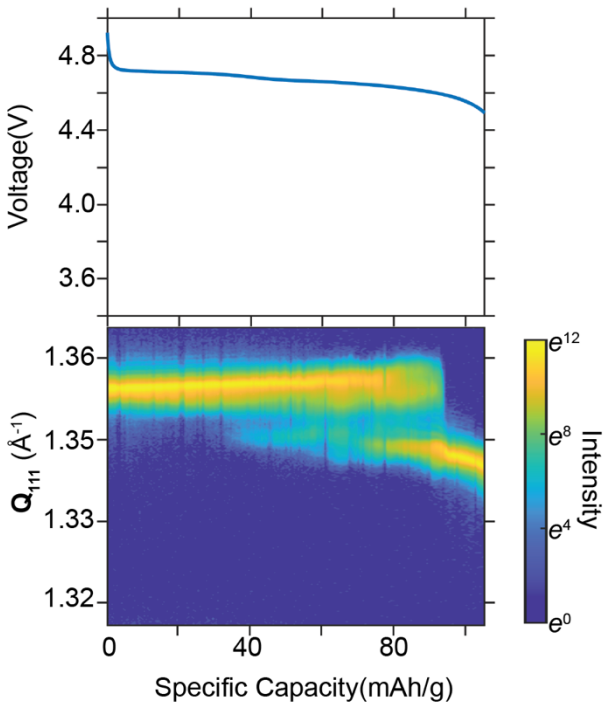

Fig. S11. Electrochemical data of another cell (top) and diffraction data of another $Li_xNi_{0.5}Mn_{1.5}O_4$ particle in the cell (bottom) that was discharged at C/10. Similar to the particle discussed above, this supplementary particle also displays an extended period of two-phase coexistence during the discharge, visible as the peak splitting in the diffraction. The two-phase region is again coincident with the voltage plateau in the electrochemical data.

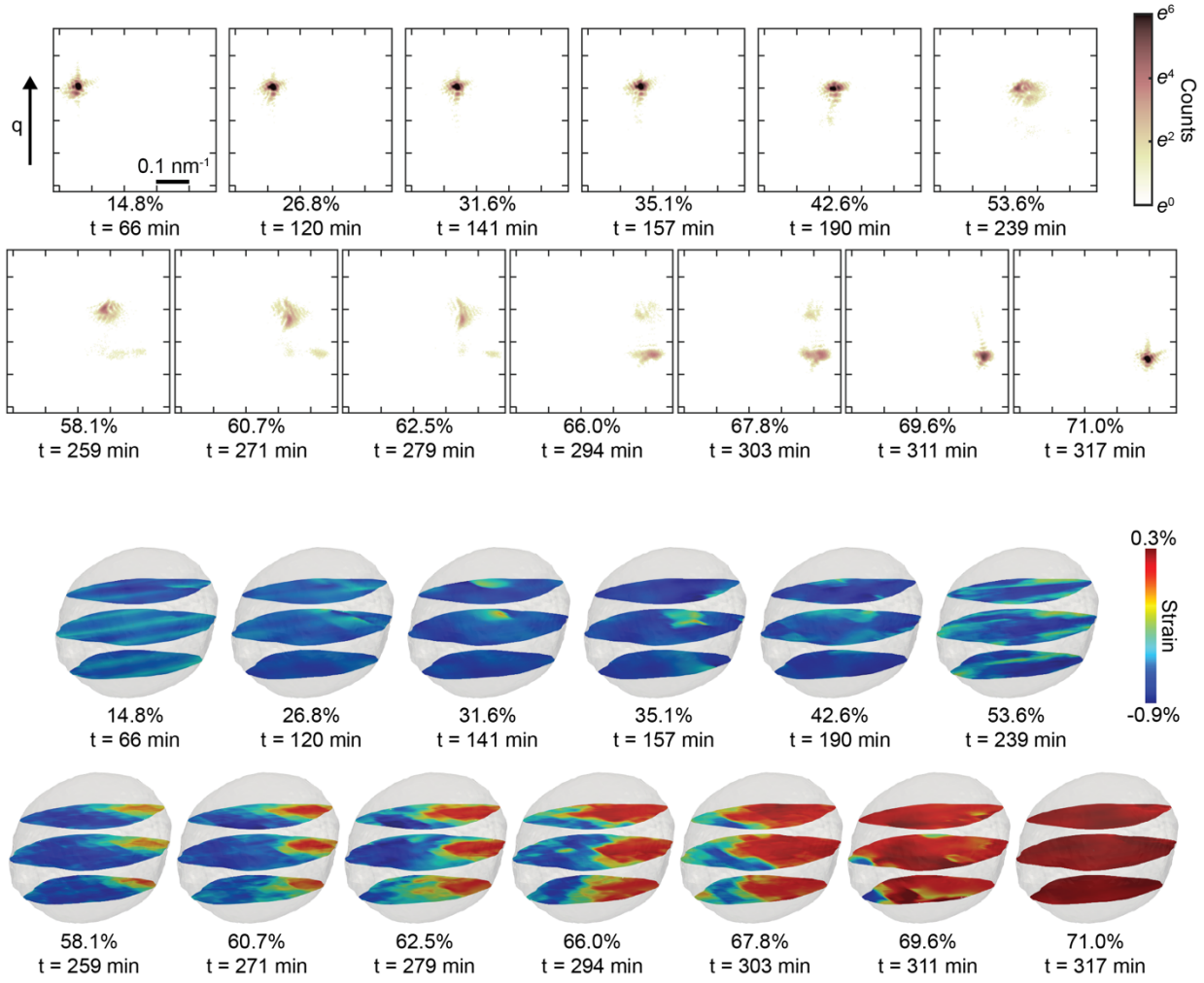

Fig. S12. 2D diffraction slices and the corresponding inverted strain maps at three chosen planes for the supplementary particle during discharge at C/10. Similar to the particle discussed above, this supplementary particle also shows a nucleation and growth regime where the nucleated Li-rich phase grows through interface propagation. The images are less smooth as they represent averages over less reconstruction runs.

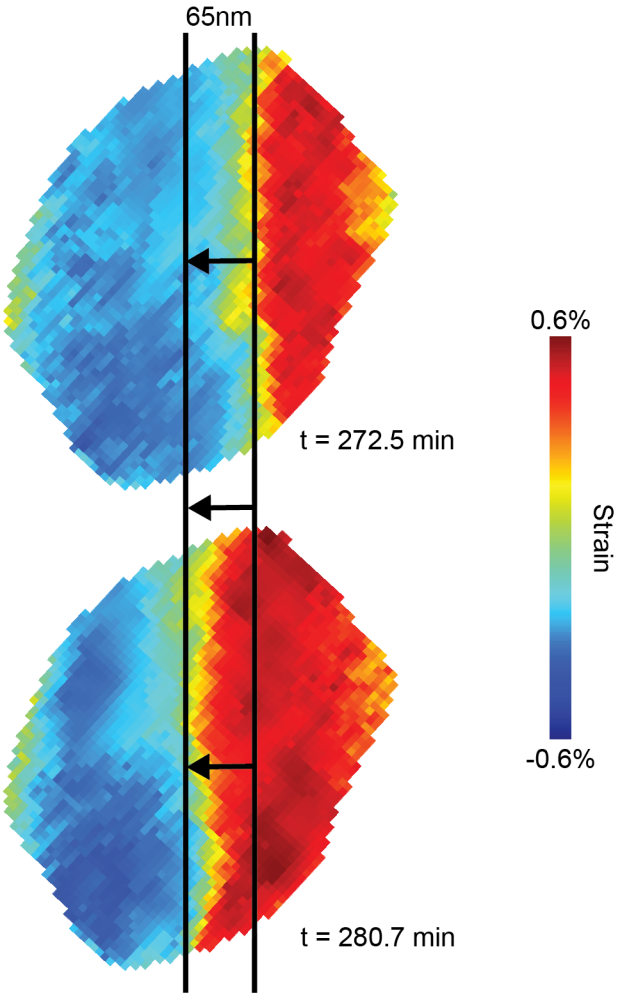

Fig. S13. Interface velocity measured during the *operando* imaging experiment. Looking at specifically the region when a linear interface exists, we approximate the distance that the interface travels to be around 65 nm in 494 seconds. In three-dimensional diffusion in spinel $Li_xNi_{0.5}Mn_{1.5}O_4$, the movement of ions can be described with mean square displacement $< x^2 > = 6Dt$, where D is the diffusion coefficient and t is the time. Using bulk diffusion coefficient of Li in $Li_xNi_{0.5}Mn_{1.5}O_4$, $D_{Li} = 2 \times 10^{-12}$ cm^2/s [4], we calculate the average distance for the given time, $x = \sqrt{6Dt} = \sqrt{6 * 2 * 10^{-12}\ \mathrm{cm^2/s} * 494\ \mathrm{s}} = 7.7 \times 10^{-5}\mathrm{cm} = 770$ nm. This is one order of magnitude larger than the 65 nm we observe. We conclude that at the discharge rate, the interface propagation is not limited by Li diffusion in the particle.

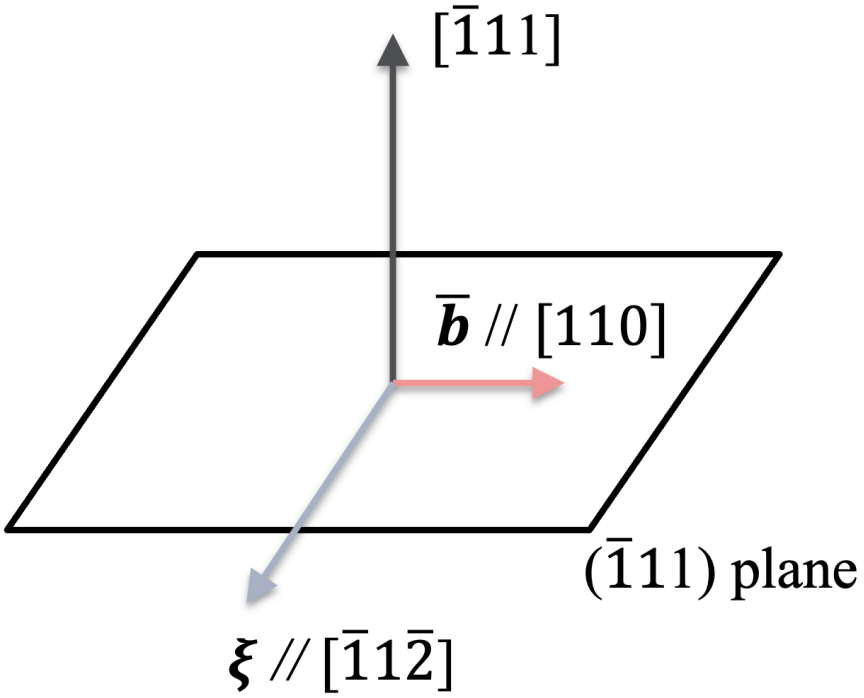

Fig. S14. Geometry of the dislocations used in microelasticity modelling. During discharge, $Li_xNi_{0.5}Mn_{1.5}O_4$ transforms from a cubic-spinel to another cubic-spinel phase with a lattice mismatch of 0.9% (consistent with literature and estimated directly from the diffraction data through peak splitting). The coherency strain is the same along all three principal axes of the <100> family. We find the stress tensor by multiplying the strain tensor with the elastic stiffness tensor. The elastic stiffness tensor was adopted from a similar spinel material $LiTi_2O_4$ [5] and assumed equal for both phases. For the semi-coherent interface to reflect the coherency loss along [110], we rotate the strain matrix along the z direction by 45 degrees to align [110] on [100] and set it to be 0, then transformed it back to the previous coordinates.

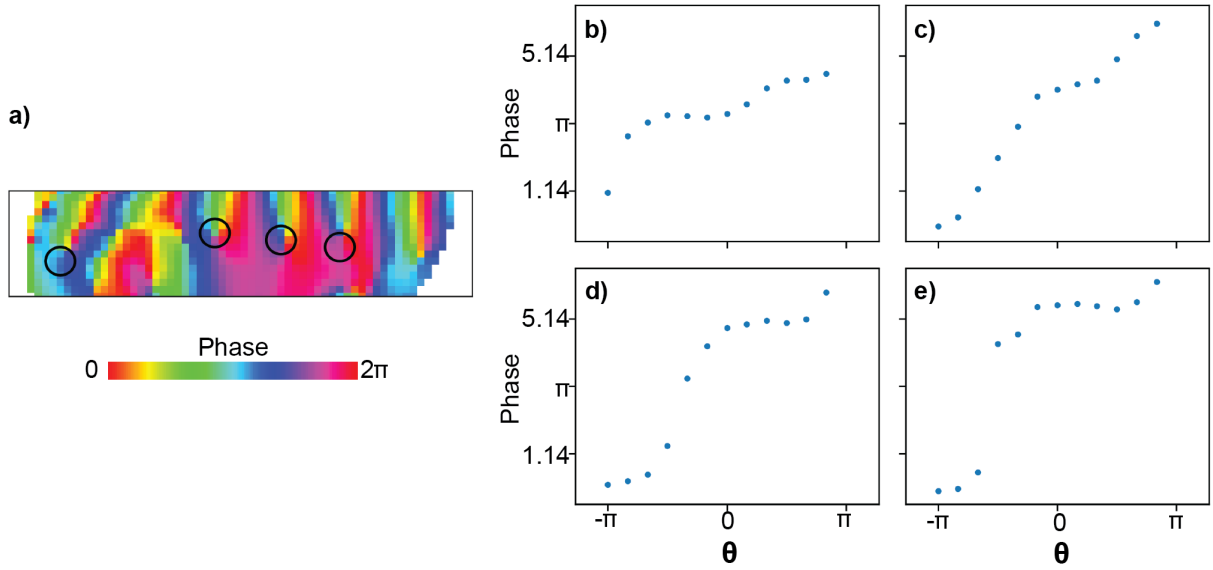

Fig. S15. Identifying singularities and the azimuthal scans indicating dislocations. a) The enlarged phase map at 58.8% DoD same as Figure 4c. **b) - e)** The azimuthal scans around the singularities as circled in **a)**. All scans show an average phase jump around 5 radians.

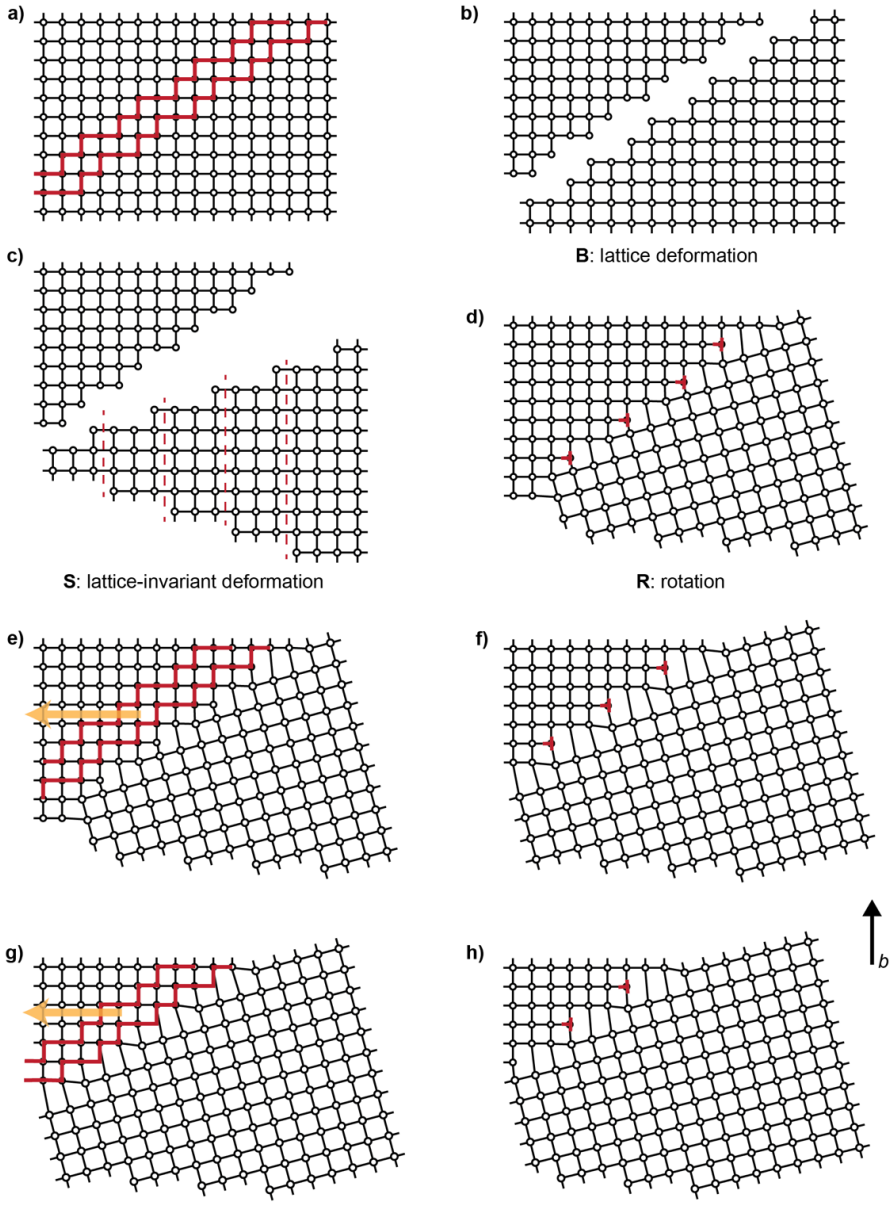

Fig. S16. 2D illustration of the creation and propagation of a glissile interface. The example shows a growth of a square structural phase with a larger lattice parameter, similar to growth of Li-rich $Li_xNi_{0.5}Mn_{1.5}O_4$ that has a cubic structure with a larger lattice parameter. The operation to minimize coherency strain at the interface includes lattice deformation ***B***, lattice-invariant shear deformation ***S***, and rotation $\boldsymbol{R}^6$. The lattice-invariant deformation introduces slip with misfit dislocations at the interface, which move along the slip planes during interface propagation. Each snapshot shows an array of dislocations (**d**, **f**, **h**). During the subsequent snapshot the dislocation array (each consisting of a different set of dislocations) moves perpendicular to the Burgers vector. This occurs via conservative motion where new dislocations enter the interface at the surface and exit the interface at the opposite surface.

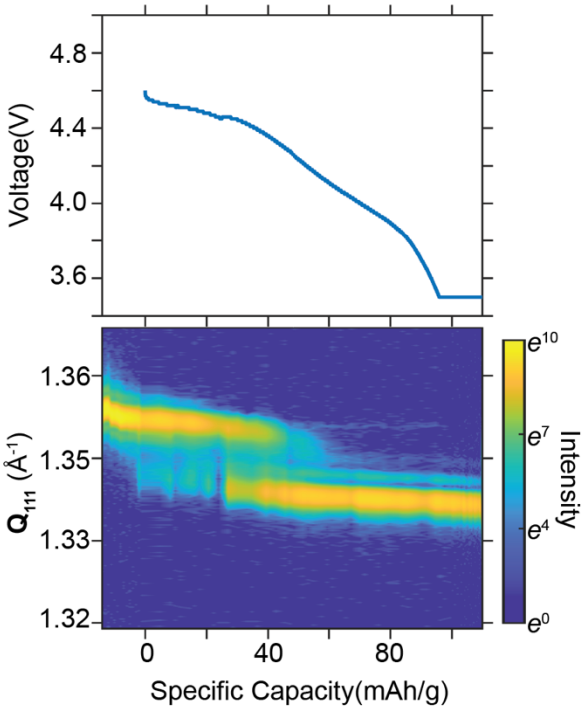

Fig. S17. Electrochemical data of the cell (top) and diffraction data of a single $Li_xNi_{0.5}Mn_{1.5}O_4$ particle within the cell (bottom) at discharge rage of C/2. The two-phase coexistence is still present at a much higher discharge rate. This supports our hypothesis that the phase separation in $Li_xNi_{0.5}Mn_{1.5}O_4$ does not necessarily limit its kinetics as dislocations play an important role in reducing energy barriers for the reaction.

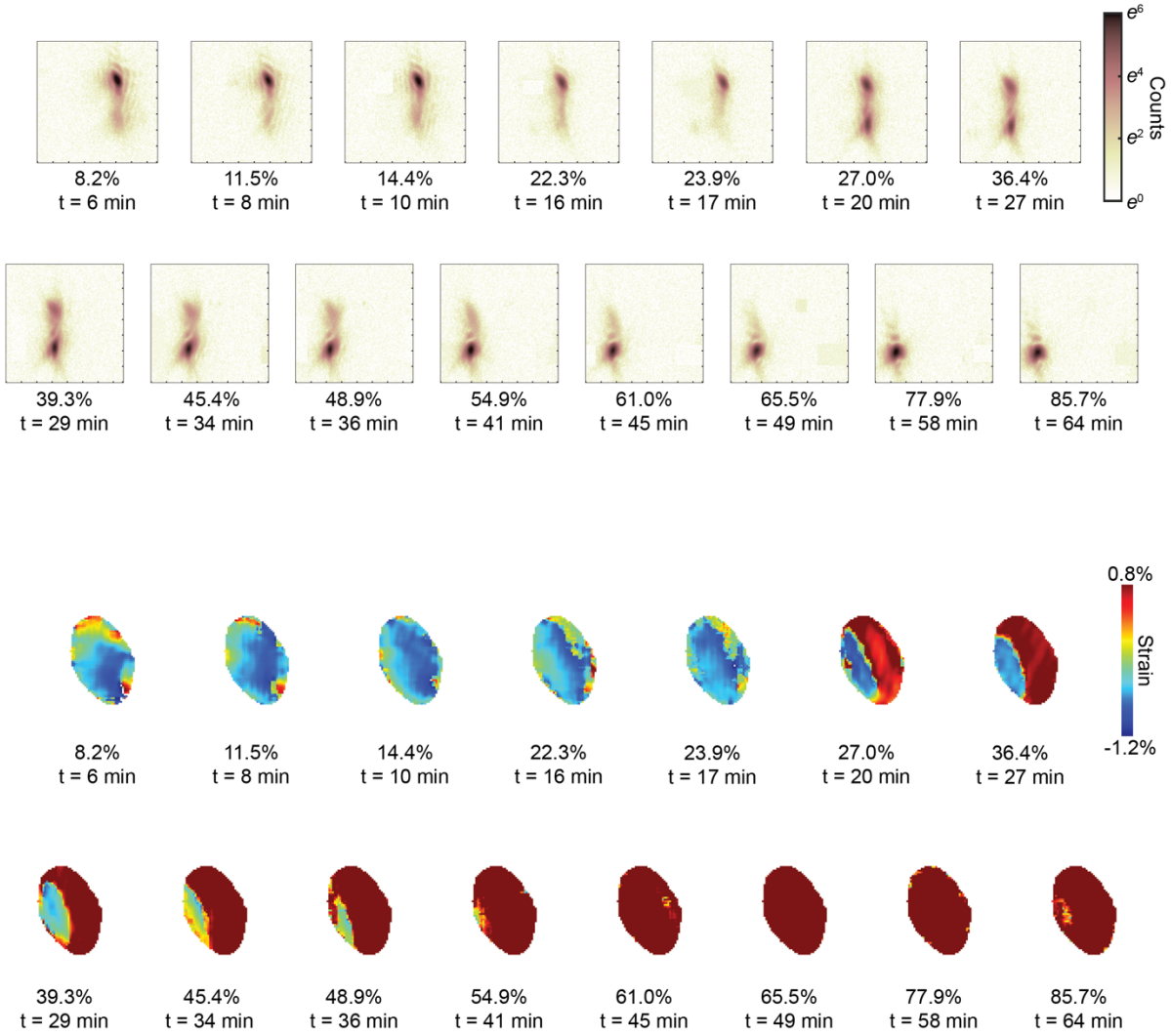

Fig. S18. Operando imaging of the structural phase transformation during discharge at C/2. Phase retrieval of the data shown in S16 and collected at a discharge rate of C/2. Akin to a slower discharge rate of C/10, nucleation and growth are visible.

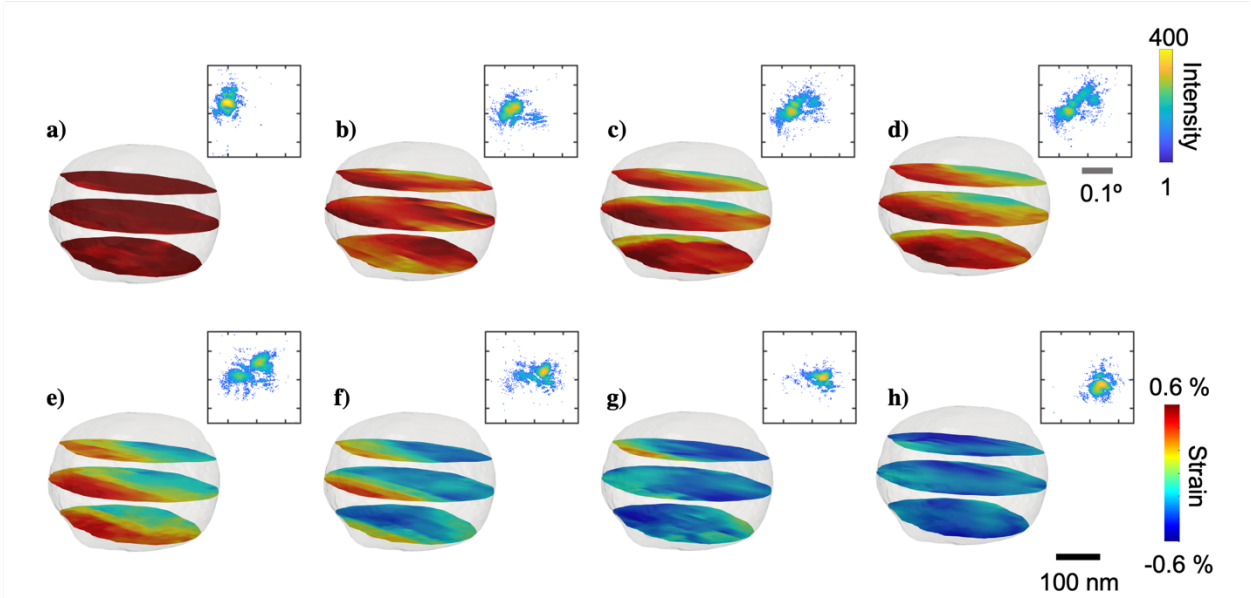

Fig. S19. Metastable solid solution during lithium extraction. (a) – (h) The 3D imaging of strain field for the two-phase reaction a LNMO nanoparticle during charge and the cross sections of the 3D diffraction pattern in each charge state. In contrast with the discharge two-phase reaction, the charge two-phase exhibits a solid-solution behavior as there is still phase separation but the strain difference is much smaller than in the discharge case. This is considered a metastable solid-solution reaction.

References

1. Williams, G. J., Pfeifer, M. A., Vartanyants, I. A. & Robinson, I. K. Three-Dimensional Imaging of Microstructure in Au Nanocrystals. *Physical Review Letters* **90**, 4 (2003).
2. Fienup, J. R. Phase retrieval algorithms: a comparison. *Appl. Opt.* **21**, 2758 (1982).
3. Luke, D. R. Relaxed averaged alternating reflections for diffraction imaging. *Inverse Problems* **21**, 37 (2004).
4. Kunduraci, M. & Amatucci, G. G. The effect of particle size and morphology on the rate capability of 4.7V LiMn1.5+δNi0.5−δO4 spinel lithium-ion battery cathodes. *Electrochimica Acta* **53**, 4193–4199 (2008).
5. Qi, Y., Hector, L. G., James, C. & Kim, K. J. Lithium Concentration Dependent Elastic Properties of Battery Electrode Materials from First Principles Calculations. *J. Electrochem. Soc.* **161**, F3010 (2014).
6. Balluffi, R. W., Allen, S. M. & Carter, W. C. *Kinetics of Materials*. (John Wiley & Sons, 2005).